Power Electronics and Drives
Volume 11(46), 2026 DOI: 10.2478/pead-2026-0013

Newton–Raphson Method-based Power Flow Decoupling for Five-port Modular Multi-Active Bridge Converters

Research paper

Tomáš Basarik[1,*], Tadeáš Kmecik[1], Daniel Gordan[1], Milan Lacko[1], Karol Kyslan[1], Anna Grinčová[2]

[1]*Department of Electrical Engineering and Mechatronics, Technical University of Košice, Košice, Slovak Republic*
[2]*Department of Mathematics and Theoretical Informatics, Technical University of Košice, Košice, Slovak Republic*

Received: 26 February, 2026; Received in the revised form: 20 April, 2026; Accepted: 21 April, 2026

Abstract: Modern energy systems require efficient power management, making multi-active bridge (MAB) converters ideal for electric vehicle (EV) charging and DC microgrids. However, higher port counts lead to magnetic coupling and non-linear dynamics, complicating independent control. This paper proposes a generalised power flow decoupling strategy for a five-port modular multi-active bridge (MMAB) converter using the Newton–Raphson (NR) method. Unlike traditional reduced-order models, a current-based model is employed to maintain modularity. A key contribution is the integration of the Moore–Penrose pseudoinverse into the NR solver to mitigate Jacobian singularities and ensure numerical stability. The algorithm is implemented on a dual-core central processing unit (CPU), achieving a deterministic 40 μs execution time. Furthermore, this study identifies performance degradation caused by parasitic inductances in the modular AC bus and proposes an optimised design using magnetic flux cancellation. Modelling precision is further refined through offline fast Fourier transform (FFT)-based parameter identification. Experimental validation on a five-port MMAB prototype confirms that the proposed method provides superior steady-state accuracy and robust dynamic decoupling during rapid transient load transitions.

Keywords: *multi-active bridge converter • power flow decoupling • Newton–Raphson method • DC microgrids • real-time control*

1. Introduction

Driven by the European Green Deal, the urgency of energy decarbonisation necessitates high-efficiency power conversion and optimised energy utilisation (European Commission, 2019). The transition towards microgrids integrated with distributed energy resources dictates a paradigm shift from conventional single-input single-output (SISO) converters to advanced multi-input multi-output (MIMO) architectures. Modern power electronics research prioritises maximising power density and mitigating switching losses via high-frequency soft-switching techniques, while maintaining energy efficiency as the benchmark performance metric (Koohi et al., 2023).

The dual active bridge (DAB) topology offers bidirectional power flow, galvanic isolation, and a wide operating voltage range. However, its integration into complex microgrids reveals scalability limitations, specifically reduced power density when interconnecting multiple nodes. To mitigate these constraints, multi-active bridge (MAB) converters have emerged as a necessary evolution (De Doncker et al., 1991). MAB architectures enable the direct coupling of multiple sources and loads, bypassing the need for intermediate power conversion stages. This structural simplification maximises power density, making MAB converters ideal for electric vehicle fast-charging stations, battery energy storage systems, and the seamless integration of renewable energy sources (Tao et al., 2008).

* *Email: tomas.basarik@tuke.sk*

Open Access. © 2026 Authors, published by Wroclaw University of Science and Technology. This is an open access article licensed under the Creative Commons Attribution License (http://creativecommons.org/licenses/by/4.0/).

The fundamental technical challenge of MAB converters lies in the strong power coupling between individual ports and the constraints of a fixed port count. Although the modular multi-active bridge (MMAB) concept (Zumel et al., 2014) introduces necessary modularity, the issue of mutual port interaction remains unresolved because of the shared AC bus. The power flow at each port is determined by the voltage difference between that node and the common bus, forming a non-linear relationship that involves the operating states of all connected ports simultaneously. Consequently, a parameter variation in a single node induces undesired power fluctuations across all other ports. Ensuring system stability and independent energy flow control requires advanced power decoupling methods to eliminate cross-coupling effects and enable autonomous port control. These strategies are currently classified into hardware-based and software-based approaches.

Hardware-based decoupling relies on minimising leakage inductance to transform a specific port into a stiff voltage source that dictates the AC bus voltage. This configuration allows the remaining ports to operate as independent DAB converters. One approach (Wang et al., 2019) employs a resonant circuit where a capacitor is added in series with the transformer's leakage inductance. When the switching frequency matches the resonant frequency, the port impedance becomes negligible. However, the effectiveness of this method is highly sensitive to the precision of resonant circuit parameters. In practice, manufacturing tolerances and limited commercial availability of precise passive components complicate implementation. Mitigating these tolerance-related issues often requires variable components, which increases both system cost and complexity (Koohi et al., 2023). Alternatively, the authors in Bandyopadhyay et al. (2021a) proposed a transformer design with minimal inherent leakage inductance, utilising external series inductors on all ports except the primary one. While this effectively neglects the main port's inductance, the use of auxiliary inductors increases overall system losses. Furthermore, this approach compromises modularity since the main port must remain operational to maintain system decoupling. In addition to transformer-based solutions, literature (Gao et al., 2025) proposes the use of a non-isolated H-bridge converter connected directly to the AC bus. This H-bridge acts as a dedicated voltage source that establishes the reference voltage for the entire bus, effectively decoupling the remaining ports without relying on minimised leakage inductance or complex resonant networks.

Software-based decoupling offers a versatile alternative to hardware-centric approaches. Early strategies for MAB converters relied primarily on linear control techniques utilising small-signal models. These systems are linearised around a specific operating point through a first-order Taylor expansion to derive a decoupling matrix that eliminates inter-port interaction. However, a significant drawback is the necessity to precompute and store decoupling matrices for an extensive range of operating points. This requirement leads to memory-intensive implementations and necessitates complex lookup table management, limiting the controller's effectiveness across highly dynamic operating ranges (Langbauer et al., 2021; Nishimoto et al., 2017; Zhao et al., 2008).

Time-sharing control represents a distinct alternative by actively controlling only two ports at any given moment while the remaining ports operate as passive rectifiers. In this configuration, the common port operating cycle exceeds the switching period and is partitioned into intervals based on the instantaneous power demands of individual output ports. Although time-sharing control enhances efficiency under light-load conditions, it significantly reduces power density as the port count increases. This degradation occurs because the converter hardware potential remains underutilised. Furthermore, discontinuous energy delivery induces substantial output voltage ripple, necessitating larger filter capacitors to maintain stability (Chen et al., 2019, 2020).

Active disturbance rejection control (ADRC) offers a robust framework for MAB converters by treating inter-port coupling, model uncertainties, and external influences as a unified system disturbance. This total disturbance is estimated and rejected in real-time, providing a decentralised control structure where design complexity remains independent of port count. Unlike methods requiring high-fidelity modelling, ADRC necessitates only the system order for implementation. In practical scenarios, linear ADRC is preferred for its straightforward microcontroller integration and simplified tuning. Its performance is primarily dictated by the bandwidth of the Extended State Observer; however, digital implementation requires careful consideration of computational delays. Consequently, controller gains must be constrained to maintain stability, often necessitating a trade-off with the maximum achievable dynamic response (Bandyopadhyay et al., 2021b; Henao-Muñoz et al., 2025; Wu et al., 2026).

The Newton–Raphson (NR) method, introduced in Wang and Chen (2018), provides a robust numerical framework for solving the non-linear power flow equations inherent to MAB converters. By iteratively updating the phase-shift vector, the algorithm identifies the optimal control variables required to meet target power or current demands across individual ports. Unlike linear techniques restricted to a single-point Taylor expansion, the NR method ensures precise decoupling across the entire operating range by minimising the residual error between actual and demanded power until it falls below a predefined tolerance. This iterative approach facilitates high-

fidelity control without the need for memory-intensive lookup tables, effectively overcoming the limitations of static linearisation (Basarik et al., 2025).

Building upon the preliminary three-port study presented in Basarik et al. (2025), this paper presents a generalised and significantly extended power flow decoupling strategy for a five-port MMAB converter, employing the NR iterative method to ensure precise control. By utilising a full current model instead of traditional reduced-order alternatives, the proposed solution preserves the inherent modularity and symmetry of the architecture. The integration of the Moore–Penrose pseudoinverse into the iterative solver prevents Jacobian matrix singularities and enhances numerical stability. Implemented on a dual-core central processing unit (CPU) architecture, the algorithm achieves a deterministic execution time of 40 µs, aligning with the converter's control period. Furthermore, the study evaluates the impact of modular AC bus parasitic inductances and introduces an optimised hardware design to mitigate these effects via magnetic flux cancellation. To refine modelling accuracy, the system incorporates offline parameter identification through fast Fourier transform (FFT) analysis. Experimental validation on a five-port prototype demonstrates high steady-state accuracy and robust dynamic decoupling during rapid load transitions.

2. Modelling of the Five-Port MMAB Converter

The five-port MMAB converter architecture, illustrated in Figure 1, is based on standardised MMAB power modules. Each module integrates a DC voltage filter, a full H-bridge, and a high-frequency transformer. These units are connected in parallel to a shared AC bus. This modular approach significantly increases power density and system flexibility compared to parallel-connected DAB converters. Power flow within the converter is managed through single phase shift (SPS) Modulation (Jauch and Biela, 2015). This method controls energy transfer by adjusting the phase angles between the square-wave voltages of the individual ports. The resulting voltage differences drive current through the leakage inductances to facilitate precise power exchange.

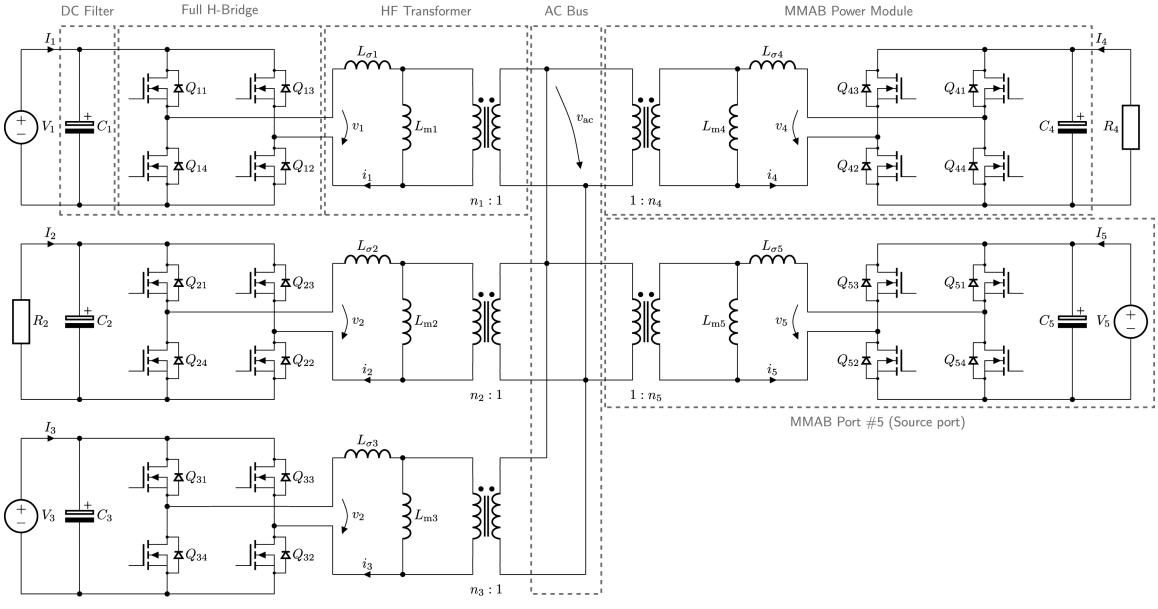

Figure 1. MMAB converter topology. MMAB, modular multi-active bridge.

Figure 2 illustrates the characteristic waveforms of the five-port MMAB converter $(k = 5)$ for a selected parameter configuration. The system operation is governed by the potential difference between the individual port voltages v_i and the common AC bus voltage v_{ac}. For each port $i \in \{1,\ldots,k\}$, the H-bridge output voltage is defined by the DC link voltage V_i and the control phase shift ϕ_i, which serves as the primary control variable for power flow control. This phase shift dictates the relative phase displacement of the rising edge on the time axis for each module. The common AC bus voltage v_{ac} is shared by all ports, with its instantaneous value determined by the superposition of

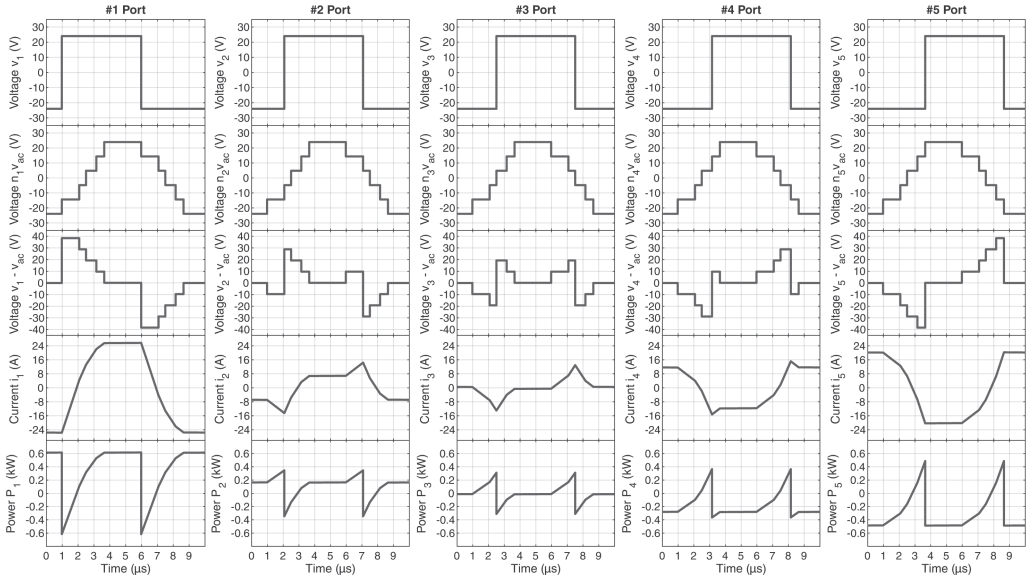

Figure 2. Typical operating waveforms of the five-port MMAB converter. The waveforms are obtained with the following parameters: $V_i = 24$ V; $L_{\sigma i} = 1.4\mu$H; $L_{\mathrm{m}i} = 600$ μH; $n_i = 6/3$; $i \in \{1,\ldots,k\}$; $\phi_1 = 0.149$; $\phi_2 = 0.039$; $\phi_3 = -0.003$; $\phi_4 = -0.068$; $\phi_5 = -0.118$; $P_1 = 360$ W; $P_2 = 120$ W; $P_3 = 0$ W; $P_4 = -180$ W; $P_5 = -300$ W. MMAB, modular multi-active bridge.

voltages from all connected power modules. The voltage across the transformer leakage inductance $L_{\sigma i}$ is expressed as the difference between the port voltage v_i and the common AC bus voltage v_{ac}. This differential voltage defines the inductor current i_i as:

$$v_i - v_{ac} = L_{\sigma i}\frac{di_i}{dt}. \tag{1}$$

The instantaneous power P_i of a single MMAB module is subsequently derived from the product of the instantaneous port voltage and the leakage inductor current. This physical relationship constitutes the fundamental mechanism for multiport power flow control within the modular architecture.

2.1. Generalised current-based power flow model

The MMAB converter is represented by a lossless equivalent circuit, illustrated in Figure 3, incorporating the leakage and magnetising inductances of the transformers. By applying Millman's theorem to the star-node of the parallel-coupled ports, the instantaneous common AC bus voltage v_{ac} is derived as:

$$v_{ac} = \frac{\sum_{i=1}^{k}\frac{v_i n_i}{L_{\sigma i}}}{\sum_{i=1}^{k}\left(\frac{n_i^2}{L_{\sigma i}} + \frac{n_i^2}{L_{mi}}\right)} = \frac{\sum_{i=1}^{k}\frac{v_i n_i}{L_{\sigma i}}}{\frac{1}{L_{eq}}}, \tag{2}$$

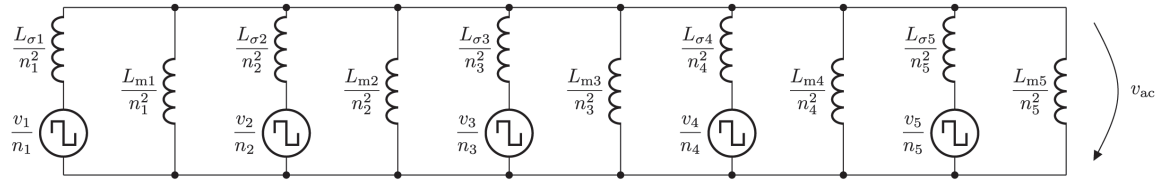

Figure 3. Lossless equivalent circuit of MMAB converter. MMAB, modular multi-active bridge.

where k denotes the total number of ports, v_i is the *i*-th port voltage, n_i represents the transformer turns ratio, and $L_{\sigma i}$ is the leakage inductance of the *i*-th port. The equivalent system inductance, L_{eq}, is derived from the parallel combination of the leakage and magnetising inductances across all integrated modules. Under the SPS modulation, introduced in Panchbhai et al. (2026), the average current I_i at a specific port is determined by the superposition of current contributions from all coupled ports. This relationship is defined as follows:

$$I_i = \sum_{\substack{j=1 \\ j \neq i}}^{k} \frac{V_j n_i n_j \left(\phi_i - \phi_j\right)\left(1 - 2\left|\phi_i - \phi_j\right|\right)}{f_s \frac{L_{\sigma i} L_{\sigma j}}{L_{eq}}}, \tag{3}$$

where V_j denotes the DC port voltage, ϕ represents the phase shift, and f_s is the switching frequency. To facilitate the decoupling algorithm design, this relationship is reformulated using an equivalent conductance G_{ij}. Consequently, the port currents are expressed in a compact matrix form:

$$\mathrm{I} = \mathrm{G}\mathrm{V}, \tag{4}$$

where the elements of the conductance matrix **G** are defined as:

$$G_{ij} = K_{ij}\phi_{ij}(1 - 2|\phi_{ij}|), \tag{5}$$

with the coupling coefficient K_{ij} and the relative phase shift ϕ_{ij} given by:

$$K_{ij} = \frac{n_i n_j}{f_s \frac{L_{\sigma i} L_{\sigma j}}{L_{eq}}}, \qquad \phi_{ij} = \phi_i - \phi_j. \tag{6}$$

In this notation, I and V are the port current and voltage vectors, respectively. The conductance matrix G encapsulates the non-linear cross-coupling dynamics between the individual ports.

2.2. Singularity analysis and Kirchhoff's constraint

The MMAB converter model is governed by Kirchhoff's current law (KCL) applied to the common star-node. Since all power modules are coupled in parallel to the shared AC bus, the algebraic sum of all currents entering the node must be zero. This physical constraint introduces inherent coupling between the k ports, implying that their power flows are not mathematically independent. From a mathematical perspective, this dependency results in a singularity within the system's characteristic matrix. In a k-port system, the rank of the conductance matrix G (and the subsequent Jacobian (J) is $k-1$, rendering the system non-invertible through standard algebraic methods. This singularity reflects the physical equilibrium requirement where any change in a single port's power flow must be balanced by the remaining $k-1$ ports to satisfy the KCL at the AC bus. To maintain system modularity and eliminate the need for a fixed reference (slack) port, a pseudoinverse-based approach is employed. By utilising the Moore–Penrose pseudoinverse (J^+) the NR algorithm can effectively handle the singular nature of the current-based power flow model. This method ensures robust numerical convergence while preserving the symmetrical control architecture across all k modules.

3. Real-Time NR Decoupling Algorithm

The lossless model of the MMAB converter, defined by Eq. (4), exhibits significant non-linear cross-coupling between individual ports. To facilitate independent port control, the decoupling strategy aims to transform the system such that the resultant transfer matrix approximates an identity matrix. This ensures a direct correspondence between the requested port current vector I_{req} and the actual average output current I, effectively eliminating coupling within the common AC bus. Since the analytical inversion of the non-linear model is not feasible, the decoupling is treated as a numerical root-finding task. The objective is to identify an optimal set of phase-shift angles that minimises the

error between the required and actual port currents. The problem is formulated as the following non-linear system of equations:

$$f(\phi) = \mathrm{I}_{req} - \mathrm{I} = 0, \tag{7}$$

where I is the current-based model derived in Eq. (4). The solution is obtained by linearising the system using the NR method, allowing for precise determination of the control variables within each switching period.

The system is solved iteratively using the NR method. In each iteration Z, the phase-shift vector ϕ is updated by a correction vector $\Delta\phi$ as follows:

$$\phi_{z+1} = \phi_z + \Delta\phi_{z,} \tag{8}$$

where the correction vector $\Delta\phi$ s derived from the current residual vector $\mathrm{I}_{req} - \mathrm{I}$. To address the singularity of the Jacobian matrix J, the Moore-–Penrose pseudoinverse J^{+} is employed:

$$\Delta\phi_z = \mathrm{J}^{+}\left(\mathrm{I}_{req} - \mathrm{I}\right) \tag{9}$$

expressed in full matrix form as:

$$\begin{bmatrix} \Delta\phi_1 \\ \Delta\phi_2 \\ \vdots \\ \Delta\phi_k \end{bmatrix} = \begin{bmatrix} \frac{\partial f_1}{\partial \phi_1} & \frac{\partial f_1}{\partial \phi_2} & \cdots & \frac{\partial f_1}{\partial \phi_k} \\ \frac{\partial f_2}{\partial \phi_1} & \frac{\partial f_2}{\partial \phi_2} & \cdots & \frac{\partial f_2}{\partial \phi_k} \\ \vdots & \vdots & \ddots & \vdots \\ \frac{\partial f_k}{\partial \phi_1} & \frac{\partial f_k}{\partial \phi_2} & \cdots & \frac{\partial f_k}{\partial \phi_k} \end{bmatrix}^{+} \begin{bmatrix} I_{1req} - I_1 \\ I_{2req} - I_2 \\ \vdots \\ I_{kreq} - I_k \end{bmatrix}. \tag{10}$$

The partial derivatives that form the Jacobian matrix J are defined as follows:

$$\frac{\partial f_i}{\partial \phi_j} = \begin{cases} V_j K_{ij}\left(4\left|\phi_{ij}\right| - 1\right) & i \neq j \\ \sum_{\substack{j=1 \\ j \neq i}}^{k} V_j K_{ij}\left(1 - 4\left|\phi_{ij}\right|\right) & i = j. \end{cases} \tag{11}$$

To ensure strictly deterministic execution and meet the real-time constraints of the discrete control loop, the algorithm performs exactly one iteration per control period. Instead of using a convergence threshold ε within a single step, the phase-shift values from the preceding period are used as the initial estimate for the current update. This approach leverages the high sampling frequency of the controller; since the system state changes incrementally between periods, the single-iteration update is sufficient to maintain tracking of the optimal operating point. Under steady-state conditions, the solution remains stationary, while during transients, the algorithm converges towards the new optimal values over a sequence of control periods. This strategy eliminates the need for unpredictable iterative loops, ensuring a constant computational load on the digital signal processor.

3.1. Handling singularity via Moore–Penrose pseudo-inverse

The Jacobian matrix J, derived from the MMAB power flow model, is inherently singular with a rank of $k-1$ due to the KCL constraints at the shared AC bus. To resolve this rank deficiency without designating a fixed reference port, the Moore–Penrose pseudo-inverse $\mathrm{J}^{+}$is employed, following the methodology described in Courrieu (2008). This approach allows the iterative update defined in Eq. (9) to yield a unique solution that minimises the Euclidean norm $\| \Delta\phi_2 \|$. This minimum-norm property is critical for maintaining modular symmetry, as it ensures that the required power adjustment is distributed symmetrically across all modules by utilising the smallest possible increments in

phase-shift angles. Furthermore, it enhances numerical stability and ensures deterministic execution within the 40 µs control window, even when the system operates near its physical limits or during aggressive load transients.

3.2. Computational optimisation for dual-core CPU

The real-time feasibility of the NR decoupling algorithm is constrained by the strict timing requirements of high-frequency switching. For the five-port MMAB converter, the decoupling and current control must be completed within a deterministic window to ensure system stability. This study utilises the MabDec library, a portable C language framework designed for power flow calculations in modular converters. The library provides a generic implementation of the current-based model and is compatible with any microcontroller unit (MCU) architecture supporting the C standard. Table 1 summarises the performance benchmarks of the MabDec library on a single-core TMS320F28379D microcontroller at 200 MHz. The source code and implementation details of the MabDec library are available on GitHub[1].

Table 1. Single-core performance benchmarks of MabDec library.

Number of ports	2	3	4	5	6	7	8
Decoupling time	10.13 us	21.24 us	36.99 us	59.58 us	88.79 us	123.63 us	168.24 us
Function geninv()	7.60 us	16.84 us	30.42 us	50.19 us	76.52 us	108.63 us	149.99 us

To meet the 40 µs execution target for the five-port system, the control implementation was optimised to leverage the dual-core architecture of the TMS320F28379D. The primary core (CPU1) manages the main interrupt service routine, which begins by sampling port voltages and currents via the analog-to-digital converter (ADC) modules. Concurrently, CPU1 updates the pulse width modulation (PWM) registers using the phase-shift values calculated in the preceding control period; this strategy ensures deterministic execution and minimises control jitter by decoupling the register update from the current calculation cycle. To eliminate synchronisation latency and ensure non-blocking execution, both cores independently calculate the phase-shift differences. Following this stage, the computational workload is executed in parallel: CPU1 determines the current residual vector $\mathrm{I}_{req} - \mathrm{I}$ and processes the individual port controllers, while CPU2 simultaneously computes the Moore–Penrose pseudoinverse of the Jacobian matrix. Once the pseudoinverse is available, CPU1 performs the final matrix multiplication to derive the new update vector $\Delta\phi$. This parallelisation scheme is illustrated in Figure 4.

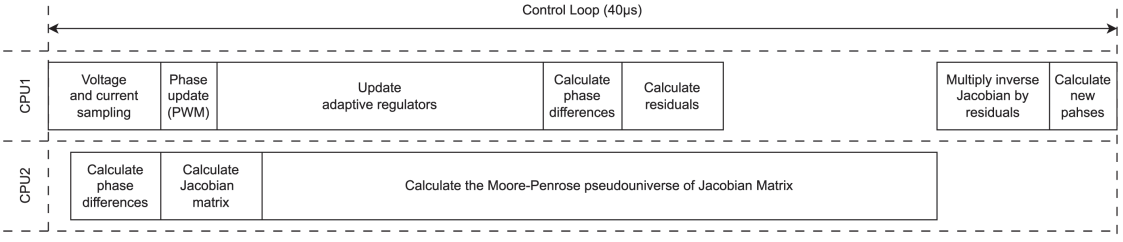

Figure 4. Parallelisation of CPU1 and CPU2.

Specific low-level optimisations were implemented to further reduce latency. The port count is fixed at $k = 5$, allowing for complete loop unrolling of the matrix multiplication cycles. Dynamic memory addressing via pointers for matrix rows and columns is replaced with strict array sizes and constant indices. Furthermore, parallel data fetching is achieved by placing critical matrices into separate physical memory blocks to prevent bus contention during simultaneous core access. These hardware-specific modifications ensure that the entire control sequence is executed within a deterministic period of 40 µs. Given the converter switching frequency of 100 kHz, the control update is performed every fourth switching cycle, resulting in a control frequency of 25 kHz. This ratio provides an optimal balance between the computational overhead of the NR iteration and the dynamic requirements of the power flow control.

1. https://github.com/tomas714/MAB-Decoupling-Newton-Raphson-Method/tree/PEAD2026.

4. Identification of Parameters and Hardware Parasitics

The accuracy of the NR decoupling algorithm depends on the precision of the identified transformer parameters and the minimisation of parasitic elements within the modular architecture. This section details the identification methodology and explores the critical impact of the AC busbar design on the validity of the star node model.

4.1. Offline identification of leakage and magnetising inductances

The magnetising inductance L_{mi} for each port is determined analytically based on the core material properties and the primary winding configuration. It is necessary to distinguish between the transformer turns ratio n_i, defined as $n_i = N_{1i} / N_{2i}$ for use in the power flow model, and the actual number of primary turns N_{1i} used for the inductance calculation. For a magnetic core with an inductance coefficient A_L, the magnetising inductance is calculated as:

$$L_{mi} = N_{1i}^2 A_{Li}. \tag{12}$$

The leakage inductances $L_{\sigma i}$ are identified experimentally using frequency domain analysis. Voltage and current measurements are conducted at the fundamental switching frequency of 100 kHz. The fundamental components of voltage V_i and current I_i are extracted via fast Fourier transform (FFT) to determine the complex impedance $Z_i = V_i / I_i$. The leakage inductance is then derived from the imaginary part of the impedance:

$$L = \frac{\mathrm{Im}(Z_i)}{2\pi f_s}. \tag{13}$$

To obtain the individual values for the star node model, a system of linear equations is constructed where the measured inductance between any two ports i and j corresponds to the sum of their respective leakage inductances $L_{\sigma i} + L_{\sigma i}$. This system is solved using the least squares approach to minimise the residual error across all possible port combinations.

4.2. Low-inductance busbar design and model validity

The standard star node model assumes that the coupling between ports occurs exclusively through the transformer inductances. However, experimental observations indicate that the physical geometry of the common AC bus introduces significant parasitic inductances that distort the power flow dynamics. In a conventional busbar layout, the loop area between the forward and return paths creates additional magnetic flux linkage.

To mitigate this effect, a low inductance busbar was designed. This implementation places the positive and negative AC paths in close physical proximity to ensure that the opposing magnetic fields cancel each other. The impact of this design choice is quantified in Figure 5. The left panel of Figure 5 displays the identification residuals for all 10 inductor combinations, comparing the original and optimised configurations. Without the low inductance design, the identification residuals show significant errors exceeding 18%. This discrepancy indicates that the star-node approximation, which assumes all ports are coupled at a single ideal point, is no longer valid due to the dominant parasitic inductance of the busbar. The right panel of Figure 5 presents the resulting identified leakage inductances for each port. After optimisation, the residuals are significantly reduced, confirming that the physical system behaviour now aligns with the mathematical model. Figure 6 illustrates the original and low inductance busbar. Table 2 summarises the final identified parameters of the five-port MMAB converter used for the experimental validation.

5. Control System Architecture

Once the system is decoupled via the NR method, each port of the MMAB converter can be treated as an independent SISO channel. This transformation allows for the implementation of decentralised voltage control. The plant transfer function $G_{s(s)}$ is defined by the parallel combination of the output filter capacitance C and the load resistance R.

$$G_{s(s)} = \frac{R}{RCs + 1} \tag{14}$$

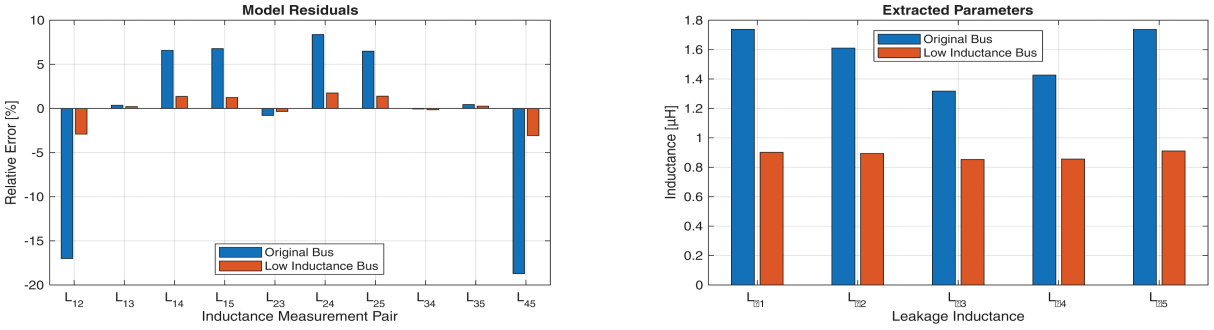

Figure 5. Graphs of relative error of identification and identified inductance.

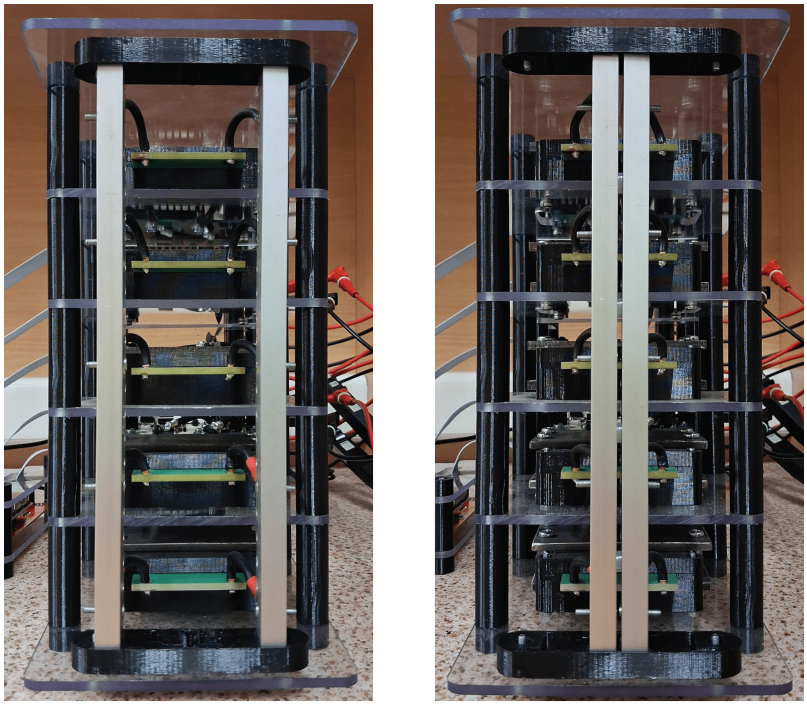

Figure 6. AC Bus: (a) Original bus; (b) Low inductance bus.

Table 2. MMAB converter nameplate parameters.

	Port #1	Port #2	Port #3	Port #4	Port #5	Unit
Maximum power	360	360	360	360	360	W
Maximum current	15	15	15	15	15	A
Nominal voltage	24	24	24	24	24	V
Leakage inductance	0.902	0.893	0.853	0.856	0.911	µH
Magnetising inductance	600	600	600	350	350	µH
Transformer ratio	6:3	6:3	6:3	6:3	6:3	-
Port capacitance	880	880	880	880	880	µF

MMAB, modular multi-active bridge.

Figure 7 illustrates the control architecture where adaptive proportional integral (PI) controllers regulate the load voltages V_2 and V_4 using real-time load resistance estimation. The current references for the source ports are determined by specific share factors (g_1, g_3, g_5) to distribute the power demand among the active energy sources. Central to the scheme is the decoupling algorithm, which translates current requests into phase shifts ϕ_i while ensuring the transfer function behaves as an identity matrix to eliminate cross-coupling. The control loop is closed through measured feedback, with source currents I_1, I_3 and I_5 being monitored for diagnostic purposes.

5.1. Adaptive PI controller design

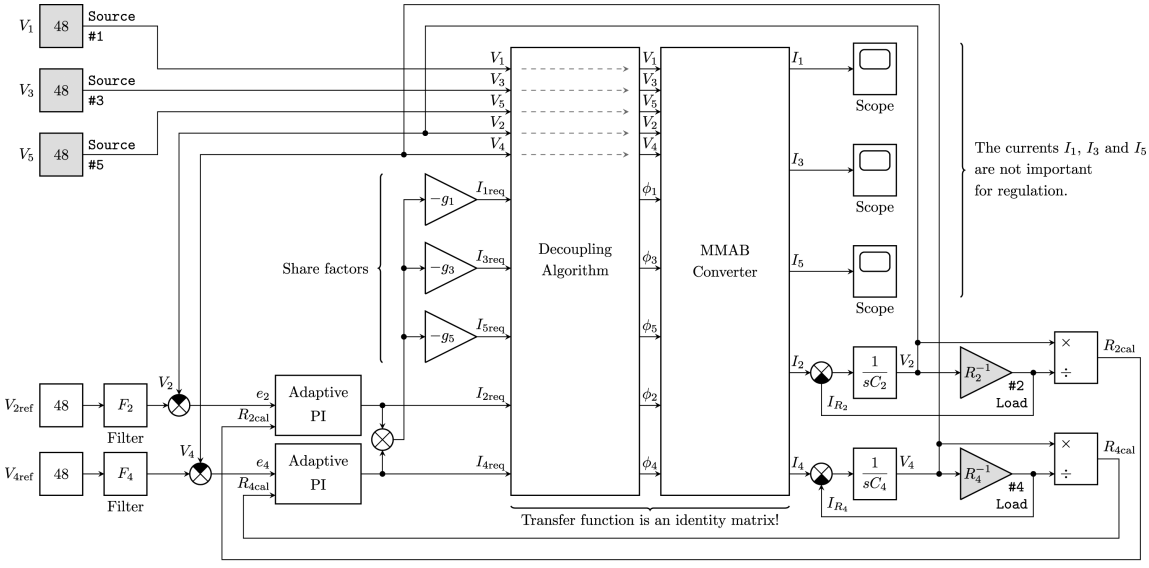

Figure 7. Block diagram of control system. MMAB, modular multi-active bridge; PI, proportional integral.

To achieve the desired dynamic response, a PI controller is designed using the pole placement method via polynomial comparison. The open loop transfer function $G_o(s)$ is formed by the product of the PI controller and the plant model:

$$G_o(s) = \frac{r_0 s + r_1}{s} G_s(s) = \frac{r_0 R s + r_1 R}{RCs^2 + s}, \tag{15}$$

where r_0 and r_1 represent the proportional and integral gains, respectively. The resulting closed loop transfer function $G_c(s)$ is then matched to a desired second-order reference model $G_r(s)$ characterised by the natural frequency ω_0 and the damping ratio ζ:

$$G_c(s) = \frac{G_o(s)}{1 + G_o(s)} = \frac{\frac{r_0}{Cs} + \frac{r_1}{C}}{s^2 + \frac{r_0 R + 1}{RCs} + \frac{r_1}{C}}, \tag{16}$$

$$G_{r(s)} = \frac{\omega_0^2}{s^2 + 2\zeta\omega_0 s + \omega_0^2}. \tag{17}$$

By equating the coefficients of the denominators in Eqs (16) and (17), the controller gains are derived as:

$$r_0 = \frac{2\zeta\omega_0 RC - 1}{R}, \quad r_1 = \omega_0^2 C. \tag{18}$$

5.2. Derivative effect suppression and real-time adaptation

The closed loop transfer function in Eq. (16) contains an additional zero, which introduces a derivative effect and potential overshoot in the step response. To neutralise this influence and ensure that the tracking performance strictly follows the reference model, an input filter $G_f(s)$ is implemented:

$$G_f(s) = \frac{\frac{r_1}{C}}{\frac{r_0}{C}s + \frac{r_1}{C}} = \frac{1}{\frac{r_0}{r_1}s + 1}. \tag{19}$$

The filter is designed to cancel the numerator of the closed loop system, thereby resulting in a pure second order response. Furthermore, since the proportional gain r_0 is a function of the load resistance R, the controller utilises an adaptive scheme. The load resistance is estimated in real-time as the ratio of the measured output voltage and current. This information is used to update the proportional gain at each control cycle, ensuring consistent damping and bandwidth across the entire operating range of the converter.

6. Experimental Results

The proposed control strategy was validated using a five-port MMAB converter prototype with a total power rating of 1.8 kW (5×360 W), shown on Figure 8. The experimental configuration consists of three source ports (Port #1, Port #3, Port #5) and two load ports (Port #2, Port #4). To demonstrate the flexibility of the modular system, the current sharing factors for the source ports were initially set to $g_1 = g_3 = g_5 = 1/3$. The voltage control was tuned for critical damping ($\zeta = 1$) with a natural frequency of $\omega_0 \approx 1160$ rad/s, aiming for a settling time of 5 ms.

To evaluate the effectiveness of the NR decoupling, sequential load steps of 10 A were applied to Port #2 and Port #4. Figure 9 (left) illustrates the system response during these transients. When a 10 A load is applied to Port #2, the voltage V_4 at the adjacent load port exhibits a peak deviation of only 104 mV (0.43%). Similarly, when Port #4 is loaded, the cross-channel interference on V_2 is limited to 94 mV (0.39%).

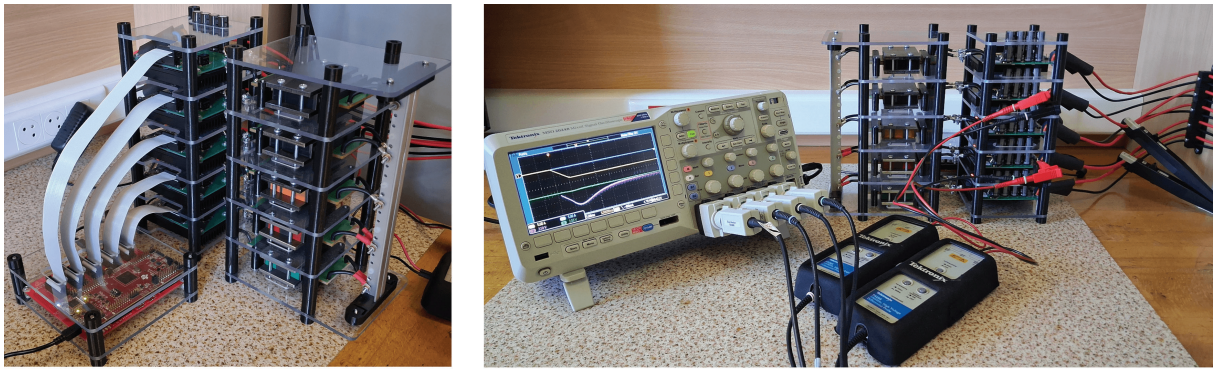

(a) (b)

Figure 8. Experimental prototype of the five-port MMAB converter: (a) detail of the DSP-based control board; (b) current and voltage sensing stage. MMAB, modular multi-active bridge. DSP, digital signal processor.

The system performance during unloading conditions was also recorded, as shown in Figure 9 (right). Upon removing the load from Port #2, the voltage V_4 experienced a transient change of 317 mV (1.32%). A similar unloading event on Port #4 resulted in a deviation of 402 mV (1.67%) on V_2. In all cases, the voltage controller successfully restored the nominal values within the targeted 5 ms window. These results confirm that the decoupling

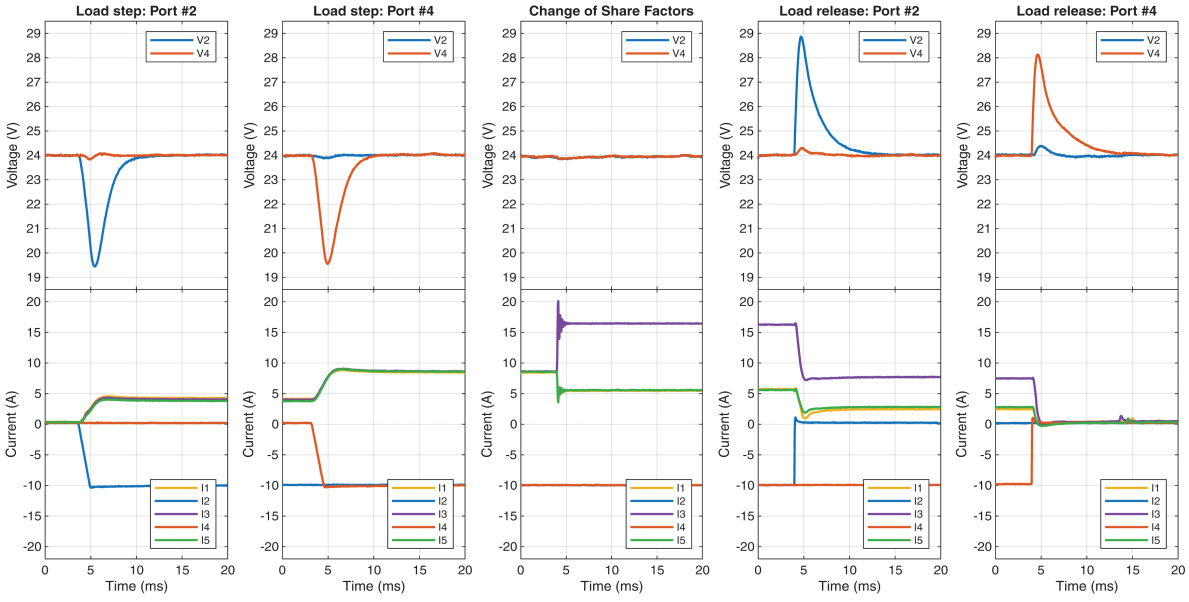

Fig. 9. Experimental results: (left) load step; (centre) share factor change; (right) load release.

algorithm effectively isolates the individual ports, preventing significant energy transfer between load channels during abrupt power changes.

As these deviations remain significantly below the 2% threshold, the non-active ports technically remain within the steady state region throughout the transient events on adjacent channels. This performance proves the high efficiency of the NR decoupling, as it effectively neutralises the magnetic coupling without triggering significant corrective actions from the secondary voltage controllers.

The modularity of the proposed solution was further tested by modifying the current sharing ratios of the source ports during operation, as seen in Figure 9 (centre). The factors g_1, g_3, g_5 were transitioned from a uniform distribution $(1/3, 1/3, 1/3)$ to an asymmetrical distribution $(1/4, 2/4, 1/4)$. The transition was observed to be instantaneous and stable, without inducing oscillations in the port voltages or violating the KCL constraints of the common AC bus, see Figure 9. This demonstrates that the Moore Penrose pseudoinverse-based solver maintains system equilibrium while allowing for arbitrary power distribution among the source modules.

7. Conclusion

This paper presented a generalised power flow decoupling strategy for a five-port MMAB converter using a real-time NR iterative method. By integrating the Moore Penrose pseudoinverse into the solver, the inherent singularities caused by KCL were successfully mitigated without the necessity of designating a fixed slack port. This approach preserves the modular symmetry of the system and ensures that all power modules operate as equal peers within the control framework. The computational optimisation for a dual core MCU architecture achieved a deterministic execution time of 40 µs, enabling a control frequency of 25 kHz which is sufficient for high dynamic control in 100 kHz switching converters.

The experimental validation confirmed that the precision of the current-based model is fundamentally linked to the hardware implementation. Specifically, the design of a low inductance AC busbar proved mandatory to align the physical system with the star node mathematical approximation. By eliminating parasitic flux linkages in the common bus, the identification residuals were minimised, allowing the decoupling algorithm to operate with high fidelity. During 10 A load transients, the system demonstrated excellent robustness, where cross-channel voltage deviations remained below 1.7% and stayed within the predefined 2% steady state error band.

These findings prove that the NR decoupling approach provides a robust and scalable solution for independent power flow control in MMAB converter topologies. The elimination of Leader/Follower dependencies and the

achievement of sub-millisecond control times make this strategy highly suitable for diverse DC microgrid applications, including hybrid energy storage systems and modular electric vehicle charging stations. Future research will focus on the integration of secondary optimisation layers to enhance system efficiency during partial load conditions.

Acknowledgements

This work was supported by the Slovak Research and Development Agency under contract No. APVV-23-0521, and by the Scientific Grant Agency of the Ministry of Education of the Slovak Republic under project VEGA 1/0584/24. This work was also funded by the European Union NextGenerationEU through the Recovery and Resilience Plan for Slovakia under project No. 09I05-03-V02-00018.

References

Bandyopadhyay, S., Purgat, P., Qin, Z. and Bauer, P. (2021a). A Multiactive Bridge Converter With Inherently Decoupled Power Flows. *IEEE Transactions on Power Electronics*, 36(2), pp. 2231–2245. doi: 10.1109/TPEL.2020.3006266

Bandyopadhyay, S., Qin, Z. and Bauer, P. (2021b). Decoupling Control of Multiactive Bridge Converters Using Linear Active Disturbance Rejection. *IEEE Transactions on Industrial Electronics*, 68(11), pp. 10688–10698. doi: 10.1109/TIE.2020.3031531

Basarik, T., Lacko, M., Grinčová, A. and Kyslan, K. (2025). Decoupling of MMAB Converter Using the Newton Iteration Method. *2025 International Conference on Electrical Drives and Power Electronics (EDPE)*, pp. 1–6. doi: 10.1109/EDPE66853.2025.11224202

Chen, Y., Wang, P., Elasser, Y. and Chen, M. (2020). Multicell Reconfigurable Multi-Input Multi-Output Energy Router Architecture. *IEEE Transactions on Power Electronics*, 35(12), pp. 13210–13224. doi: 10.1109/TPEL.2020.2996199

Chen, Y., Wang, P., Li, H. and Chen, M. (2019). Power Flow Control in Multi-Active-Bridge Converters: Theories and Applications. *2019 IEEE Applied Power Electronics Conference and Exposition (APEC)*, pp. 1500–1507. doi: 10.1109/APEC.2019.8722122

Courrieu, P. (2008). *Fast Computation of Moore–Penrose Inverse Matrices*. Available at: https://arxiv.org/abs/0804.4809, [Accessed: 25-Feb-2026]

De Doncker, R. W. A. A., Divan, D. M. and Kheraluwala, M. H. (1991). A Three-Phase Soft-Switched High-Power-Density DC/DC Converter for High-Power Applications. *IEEE Transactions on Industry Applications*, 27(1), pp. 63–73. doi: 10.1109/28.67533

European Commission. (2019). *The European Green Deal*. European Commission. Available at: https://eur-lex.europa.eu/legal-content/EN/TXT/?uri=CELEX:52019DC0640, [Accessed: 25-Feb-2026].

Gao, C., Li, K., Zhang, Z., Yuan, F., Zhang, S. and You, X. (2025). Research on Power Decoupling and Optimal Control of Modular Multiactive Bridge Converter With Relay Port. *IEEE Transactions on Power Electronics*, 40(4), pp. 5292–5308. doi: 10.1109/TPEL.2024.3506745

Henao-Muñoz, A. C., Debbat, M. B., Pepiciello, A. and Domínguez-García, J. L. (2025). Triple Active Bridge Modeling and Decoupling Control. *Electronics*, 14(21). doi: 10.3390/electronics14214224

Jauch, F. and Biela, J. (2015). Generalized Modeling and Optimization of a Bidirectional Dual Active Bridge DC-DC Converter Including Frequency Variation. *IEEJ Journal of Industry Applications*, 4(5), pp. 593–601. doi: 10.1541/ieejjia.4.593

Koohi, P., Watson, A. J., Clare, J. C., Soeiro, T. B. and Wheeler, P. W. (2023). A Survey on Multi-Active Bridge DC-DC Converters: Power Flow Decoupling Techniques, Applications, and Challenges. *Energies*, 16(16). doi: 10.3390/en16165927

Langbauer, T., Connaughton, A., Vollmaier, F., Pajnic, M. and Krischan, K. (2021). Closed-Loop Control of a Three-Port Series Resonant Converter. *2021 IEEE 22nd Workshop on Control and Modelling of Power Electronics (COMPEL)*, pp. 1–7. doi: 10.1109/COMPEL52922.2021.9646070

Nishimoto, K., Kado, Y., Kasashima, R., Nakagawa, S. and Wada, K. (2017). Decoupling Power Flow Control System in Triple Active Bridge Converter Rated at 400 V, 10 kW, and 20 kHz. *2017 IEEE 8th International Symposium on Power Electronics for Distributed Generation Systems (PEDG)*, pp. 1–6. doi: 10.1109/PEDG.2017.7972468

Panchbhai, A., Chilakalapudi, G. and Kumar, A. (2026). Impact of Single Phase Shift and Dual Phase

Shift Control Strategies on Power Decoupling in Triple Active Bridge Converter. *IEEE Transactions on Industry Applications*, 62(1), pp. 1249–1257. doi: 10.1109/TIA.2025.3595129

Tao, H., Kotsopoulos, A., Duarte, J. L. and Hendrix, M. A. (2008). Transformer-Coupled Multiport ZVS Bidirectional DC–DC Converter With Wide Input Range. *IEEE Transactions on Power Electronics*, 23(2), pp. 771–781. doi: 10.1109/TPEL.2007.915129

Wang, P. and Chen, M. (2018). Towards Power FPGA: Architecture, Modeling and Control of Multiport Power Converters. *2018 IEEE 19th Workshop on Control and Modeling for Power Electronics (COMPEL)*, pp. 1–8. doi: 10.1109/COMPEL.2018.8460019

Wang, P., Lu, X., Wang, W. and Xu, D. (2019). Hardware Decoupling and Autonomous Control of Series-Resonance-Based Three-Port Converters in DC Microgrids. *IEEE Transactions on Industry Applications*, 55(4), pp. 3901–3914. doi: 10.1109/TIA.2019.2906112

Wu, H., Lin, W., Chen, Y., Guo, H., Zhou, M. and Yang, R. (2026). Study of the Active Disturbance Rejection Control for the Decentralized Mult-Active Bridge Converter. *IEEE Transactions on Industry Applications*, 62(1), pp. 1493–1504. doi: 10.1109/TIA.2025.3603514

Zhao, C., Round, S. D. and Kolar, J. W. (2008). An Isolated Three-Port Bidirectional DC-DC Converter With Decoupled Power Flow Management. *IEEE Transactions on Power Electronics*, 23(5), pp. 2443–2453. doi: 10.1109/TPEL.2008.2002056

Zumel, P., Fernandez, C., Lazaro, A., Sanz, M. and Barrado, A. (2014). Overall Analysis of a Modular Multi Active Bridge Converter. *2014 IEEE 15th Workshop on Control and Modeling for Power Electronics (COMPEL)*, pp. 1–9. doi: 10.1109/COMPEL.2014.6877198